Journal of Zhejiang University-SCIENCE A (Applied Physics & Engineering)
ISSN 1673-565X (Print); ISSN 1862-1775 (Online)
www.jzus.zju.edu.cn; www.springerlink.com
E-mail: jzus@zju.edu.cn

Comparison of different cellular structures for the design of selective laser melting parts through the application of a new lightweight parametric optimisation method

Rubén PAZ[†1], Mario D. MONZÓN[1], Philippe BERTRAND[2], Alexey SOVA[2]

[1]*Universidad de Las Palmas de Gran Canaria, Departamento de Ingeniería Mecánica, Las Palmas de Gran Canaria 35017, Spain*

[2]*University of Lyon, ENISE, LTDS CNRS UMR 5513, Saint-Etienne 42023, France*

[†]E-mail: ruben.paz@ulpgc.es

Received July 14, 2018; Revision accepted Nov. 2, 2018; Crosschecked Dec. 6, 2018; Published online Jan. 17, 2019

Abstract: Interest in lightweight geometries and cellular structures has increased due to the freeform capabilities of additive manufacturing technologies. In this paper, six different cellular structures were designed and parameterised with three design variables to carry out the lightweight optimisation of an initial solid sample. According to the limitations of conventional computer-aided design (CAD) software, a new parametric optimisation method was implemented and used to optimise these six types of structures. The best one in terms of optimisation time and stiffness was parameterised with nine design variables, changing the dimensions of the internal cellular structure and the reinforcement zones. These seven optimised geometries were manufactured in a Phenix ProX200 selective laser melting machine without using support. The samples obtained were tested under flexural load. The results show that the cubic cell structures have some advantages in terms of CAD definition, parameterisation and optimisation time because of their simpler geometry. However, from the flexural test results it can be concluded that this type of cell structure and those with horizontal bars experience a loss of stiffness compared to the estimates of the finite element analysis because of imperfections in the manufacturing process of hanging structures.

Key words: Parametric optimisation; Cellular structures; Selective laser melting (SLM); Finite element analysis; Design of experiments; Refinement

https://doi.org/10.1631/jzus.A1800422 **CLC number:** TH164; TG665

1 Introduction

The improvement of additive manufacturing (AM) systems has led to a great uptake of these technologies in industry (Gibson et al., 2009; Wong and Hernandez, 2012; Wohlers and Caffrey, 2014). AM is defined as a "process of joining materials to make parts from 3D model data, usually layer upon layer, as opposed to subtractive manufacturing and formative manufacturing methodologies" (ISO/ASTM International, 2015). It allows the fabrication of complex geometries (even with internal hollows) that can be costly or impossible to produce with conventional manufacturing procedures.

Taking into account the capabilities of AM technologies to create internal structures, the possibilities of these technologies regarding lightweight optimisation have become an interesting challenge for AM users. The application of internal cellular structures in additive-manufactured parts can lead to lighter designs, which means more efficient parts and lower production time and cost (reduction of time and material costs).

This study is focused on the application and optimisation of cellular structures to design lightened parts for selective laser melting (SLM) technology.

ORCID: Rubén PAZ, https://orcid.org/0000-0003-1223-7067

This technology belongs in the powder bed fusion process category of AM. It consists of a thermal energy that selectively fuses regions of a powder bed. In the case of SLM, metal or ceramic powders are used (Yap et al., 2015; Protasov et al., 2017; Sing et al., 2017; Zhang et al., 2018) and the thermal energy is provided by a laser. Conventional 3D computer-aided design (CAD) software and finite element method (FEM) tools, usually available within CAD software, are used to accomplish the optimisation. FEM is used to simulate the mechanical behaviour of the different designs evaluated during the optimisation process. That enables weight minimization while keeping the minimal mechanical properties required for the part. In this case, a parametric optimisation is carried out. Although topology optimisation (available in most FEM software) (Akin and Arjona-Baez, 2001; Siemens PLM Software, 2010; Aremu et al., 2013; Kulkarni and Tambe, 2013; Lynch et al., 2013) can achieve better results than parametric optimisation, it may lead to geometries that cannot be manufactured by SLM. To overcome these limitations of topology optimisation tools, Salmi et al. (2018) proposed a methodology in which they first apply a topology optimisation and then a manual redesign to overcome the manufacturing constraints. A final FEM simulation is then required to check that the design complies with the optimisation constraints (otherwise, it should be modified again). All these steps must be carried out by the designer. However, by applying an appropriate parameterisation and controlling the interval of each design variable, it is possible to optimise the geometry and, at the same time, obtain an optimum design that can actually be manufactured. Several programs have been developed during the last decade to take advantage of AM capabilities, including tools to easily define cellular structures (Autodesk, 2015; Autodesk Within, 2015; Materialise 3-matic, 2015; Synopsys, 2015), and some of them even have FEM and optimisation tools. However, the manufacturing constraints of SLM technology cannot be easily controlled with this type of software when the optimisation of the cellular structure is carried out. Additionally, many AM users still work with conventional 3D CAD software despite the limitations or inability of such software in generating cellular structures.

Among the wide range of AM technologies available in the market, those based on powder bed have some advantages in creating hanging structures without support material since the powder bed acts as the support itself. However, there are some difficulties that must be considered. In the case of SLM, a high powered laser melts a metallic powder layer upon layer. When the powder is melted without support, the combination of low consistency of the powder beneath the layer and the high powered laser can result in bad surface finishing. Moreover, in certain circumstances, the powder feeding roller can displace the new layer if there are no supports. For this reason, hanging geometries are usually avoided in SLM designs.

This type of cellular structures for metallic AM technologies has been of interest in the field of biomedical applications (Yang et al., 2001; Sachlos and Czernuszka, 2003; Hutmacher et al., 2004; Yeong et al., 2004; Jorge et al., 2007; Peltola et al., 2008; Mullen et al., 2009; Murr et al., 2010; Yoo, 2011). However, this idea can be applied in many other sectors to benefit from the advantages of lighter-weighted parts (Dotcheva et al., 2009).

This paper combines different tools (CAD, FEM, and parametric optimisation) to accomplish a lightweight parametric optimisation for SLM parts. The CAD tool enables the definition of complex structures inside any part. The FEM enables the determination of the mechanical properties of any design (Pepelnjak et al., 2001) according to the actual boundary conditions. Finally, the developed optimisation method combines both tools to optimise the design. The entire process is automated via the application programming interface (API) of the CAD/FEM software through Visual Basic code. Therefore, the presented methodology is based on a parametric optimisation, which means that with a correct parameterisation of the design variables and intervals, the methodology will lead to designs that can actually overcame any manufacturing constraints. Although the solution achieved may be less efficient compared to the topology optimisation, the main advantage is that the presented method is automated (it only needs the correct initial set up of the parameters and FEM analysis) and manufacturability is guaranteed. On the other hand, there are some optimisation problems in which the external surface must be kept (e.g. aerodynamic components). In those cases, topology optimisation can be applied to optimise the internal

surface but it may lead to unfeasible solutions (holes with trapped powder, overhanging structures, too thin walls, etc.). In contrast, all these limitations can be controlled with the presented methodology, thus guaranteeing the manufacturability of the part.

2 Methods

2.1 Type of cellular structures applied

Different types of cellular structures are proposed in this study. Square bars are preferred compared to circular bars as they require a lower number of mesh nodes, more accurate and simple triangulation files (STL), and simpler laser paths. In all cases, the design strategies to define the internal structure (applicable in any geometry) were the following (Fig. 1):

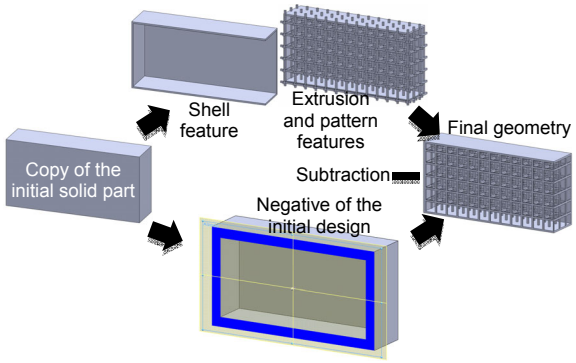

Fig. 1 CAD strategy followed to define the internal structure and keep the external surface

1. The initial solid design is used to obtain a shell and a negative of the initial geometry.

2. The pattern structure is defined using extrusion-based features.

3. Once the pattern of the internal structure is created, it is repeated along the three Cartesian axes all over the geometry to generate the internal structure, overpassing the dimensions of the initial part. This cellular structure is merged with the shell of the initial geometry.

4. The negative of the initial design is subtracted to eliminate the excess of the cellular structure, thus obtaining the initial solid design with an external skin and an internal cellular structure.

2.2 Sample geometry

The sample geometry for the analysis was a square prism of 10 mm×10 mm×70 mm, with a flexural load of 4000 N and two supports separated 60 mm (Fig. 2). The diameter of the punch and supports was 10 mm.

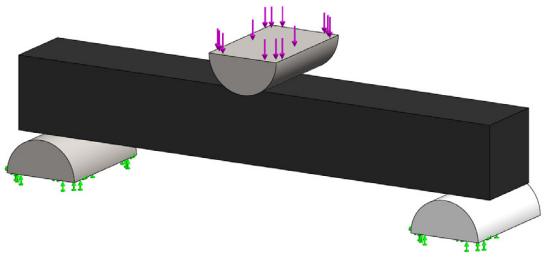

Fig. 2 Sample geometry and load conditions

Double symmetry was applied to carry out the simulations (Fig. 3). Therefore, the force was divided by four and the displacements on the symmetry faces were constrained in the normal direction. On the other hand, the lower face of the support was fixed and two contact conditions were defined, one for the contact between the round face of the support and the lower face of the part, and another one for the round face of the punch tool and the upper surface of the part (non-penetration contact). "Node to surface meshing" was applied as it achieves better results when the contact area is low (González, 2010; Dassault Systèmes, 2013). This consists of applying the contact between the node or line of one of the components and the nodes of a small area of the other component.

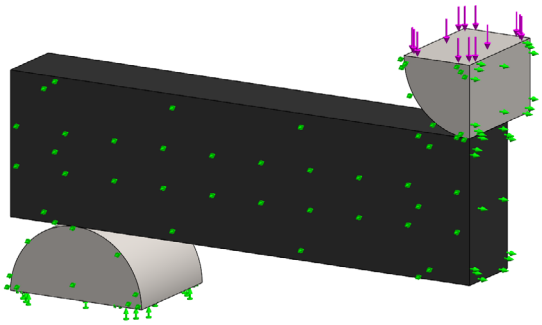

Fig. 3 Model with double symmetry for carrying out the finite element (FE) simulations

All the external surfaces of the part were kept (0.49 mm thickness) except the ends to remove the powder (Fig. 4). This methodology is especially

appropriate for the lightweight optimisation of parts whose external surface cannot be modified (e.g. aerodynamic components). For this reason, all the external surfaces were removed except the ends.

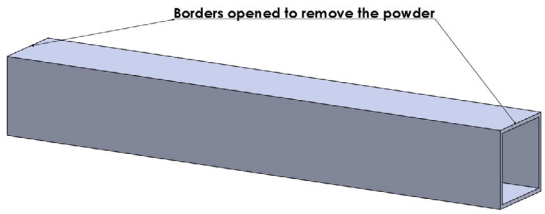

Fig. 4 Sample geometry with borders opened to remove the support material

The goal is to minimise the weight and keep the stiffness higher than 43% of the solid geometry, which is approximately the mean stiffness value of the solid part (Fig. 2) and the shell part (Fig. 4). Therefore, the optimisation constraint is related to the vertical displacement of the punch (deflection).

2.3 Cellular patterns and parameterisation

Six different types of cell geometries were proposed, all of them with a total of three design variables. These cellular structures were defined according to the following sequence (Fig. 5).

Cell 1: Simple cubic (Fig. 5a).

Cell 2: Cross lattice (Fig. 5b).

Cell 3: Cross lattice with only one bar in the cross section, the bar from the top to the laterals of the sample (following the load transmission) (Fig. 5c).

Cell 4: Cross lattice with only one bar in the longitudinal section, the bar from the top to the ends of the sample (following the load transmission towards the supports) (Fig. 5d).

Cell 5: Cross lattice and simple cubic combination, the longitudinal horizontal bars from the simple cubic cell, and the cross bars top-lateral and top-end from the cross lattice cell (load transmission towards the support and laterals of the sample) (Fig. 5e).

Cell 6: Cross lattice and simple cubic combination, the vertical bar from the simple cubic cell and the cross bars top-lateral and top-end from the cross lattice cell (load transmission towards the support and laterals of the sample) (Fig. 5f).

According to literature reviews (Thomas, 2009; Campanelli et al., 2010; Kranz et al., 2015) and the experience of the authors regarding the capabilities of SLM technology, the parameterisation and limits of the design variables were defined to keep the next list of constraints in the design.

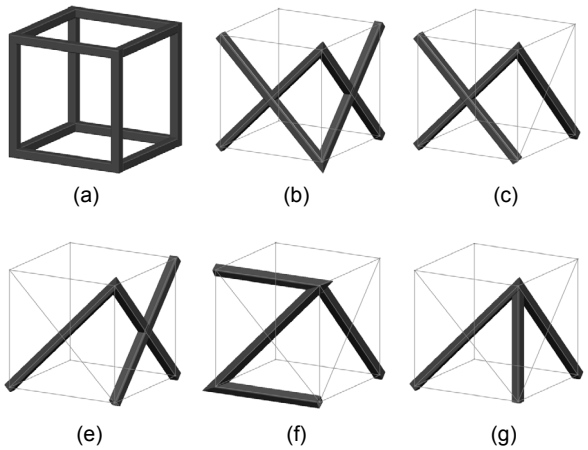

Fig. 5 Cell geometries used

(a) Simple cubic; (b) Cross lattice; (c) Cross lattice with only one bar in the cross section; (d) Cross lattice with only one bar in the longitudinal section; (e) Top-lateral and top-end from the cross lattice and longitudinal horizontal bars from the simple cubic; (f) Top-lateral and top-end from the cross lattice and vertical bar from the simple cubic

1. The distance between bars will be at least 1 mm to be able to remove the powder from the inside of the part.

2. The distance between bars will be kept lower than 2 mm to avoid problems of hanging structures in the manufacturing process.

3. The minimum angle of the bars (except for geometries with horizontal bars) will be 45° to avoid manufacturing problems in the hanging structures.

4. The side of the square bars will not be lower than 0.5 mm to guarantee good definition of the bars.

2.3.1 Cell 1 (reticular structure)

The first cellular structure pattern was a simple cubic structure (Fig. 6). The definition of the geometry was carried out by the extrusion of a matrix of squares in each Cartesian direction (Fig. 7). The main advantage of this cellular structure is that the CAD definition and parameterisation is very simple. However, bars parallel to the horizontal plane involve more difficulties in the manufacturing process (hanging structures). The design variables were the side of the square bars (VAR1), the distance between bars in the X and Y directions (VAR2, the same

distance in the *X* and *Y* axes), and the distance between bars in the *Z* direction (VAR3) (Fig. 6). The limits of each variable are shown in Table 1.

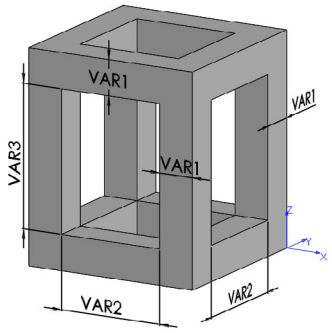

Fig. 6 Cell 1 (reticular structure)

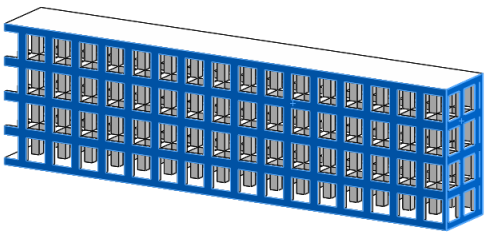

Fig. 7 Sample model with internal structure according to cell 1

Table 1 Design variables and intervals for the sample with internal structure according to cell 1

Design variable	Minimum value	Maximum value
VAR1 (mm)	0.5	1.5
VAR2 (mm)	1	2
VAR3 (mm)	1	3

2.3.2 Cell 2 (four cross bars)

The second type of cellular structure consists of four cross bars (Fig. 8). The final geometry (Fig. 9) was achieved by applying the steps listed in Fig. 1.

The design variables were the side of the square bars in the horizontal projection (VAR1), the distance between bars in the *XY* plane without taking into account the thickness of the bars in the other direction (VAR2, the same distance in the *X* and *Y* axes), and an additional value to the distance between bars in the *Z* direction (VAR3). Therefore, the distance between bars in the *X* or *Y* direction is calculated as the sum of 'VAR2' and 'VAR1' (VAR1+VAR2). The addition of 'VAR1' is needed to take into account the thickness of the bars in the normal direction, to avoid non-interconnected hollows. On the other hand, the separation between bars in the *Z* direction is calculated adding 'VAR3' to the separation between bars in the *X* or *Y* axe. Therefore, the distance between bars in the vertical direction is calculated as the sum of the three design variables (VAR1+VAR2+VAR3).

Regarding the limits of the design variables (Table 2), 'VAR1' was maintained. In the case of 'VAR2', the minimum value was set to 1 mm to guarantee at least 1 mm separation between bars (to be able to remove the powder) and the maximum was set to 2 mm (to avoid more than 2 mm between bars). 'VAR3' varies from 0 to 2 mm, which means that the distance between bars in the *Z* direction will be always equal to or higher than the distance between bars in the *XY* plane (consequently, the inclination of the bars relative to the horizontal plane will be always equal to or higher than 45°).

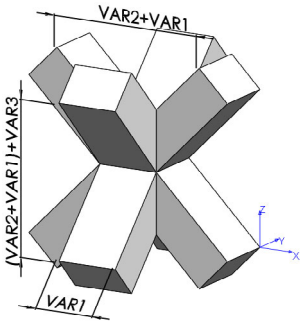

Fig. 8 Cell 2 (four cross bars)

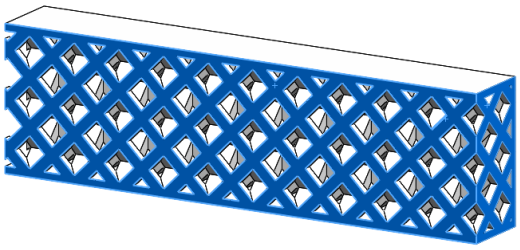

Fig. 9 Sample model with internal structure according to cell 2

Table 2 Design variables and intervals for the sample with internal structure according to cell 2

Design variable	Minimum value	Maximum value
VAR1 (mm)	0.5	1.5
VAR2 (mm)	1	2
VAR3 (mm)	0	2

2.3.3 Cell 3 (two cross bars in the longitudinal direction and one cross bar in the transversal direction)

The third type of cellular structure was similar to the previous one but keeping only one bar in the transverse plane (Fig. 10). The same features were applied to generate the lightened geometry (Fig. 11). The parameterisation was carried out in a different way compared to the previous geometry because the minimum distance between bars can be now controlled without taking into account the side of the bars. For this reason, the separation between bars in the *X* and *Y* axes was parameterised with 'VAR2', while the distance between bars in the *Z* direction was controlled by 'VAR2+VAR3', with 'VAR3' being the same addition value for the separation between bars in the vertical direction. 'VAR1' was again the side of the square bars in the horizontal projection. The limits of the design variables were the same as in cell 2 (Table 2).

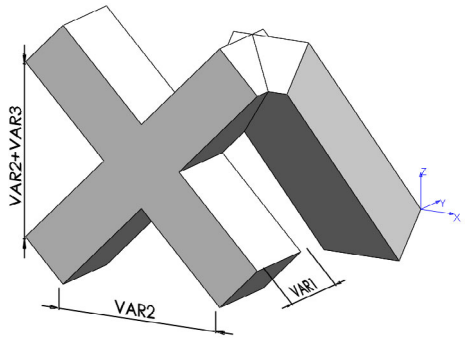

Fig. 10 Cell 3 (two cross bars in the longitudinal direction and one cross bar in the transversal direction)

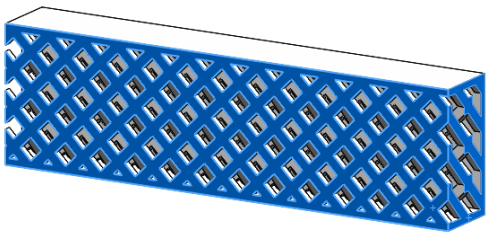

Fig. 11 Sample model with internal structure according to cell 3

2.3.4 Cell 4 (two cross bars in transversal direction and one cross bar in longitudinal direction)

In this case, only one cross bar was allocated in the longitudinal direction, while in the transversal direction the two bars of cell 2 were kept (Fig. 12). Fig. 13 shows the result of applying this cell pattern. The design variables and limits were the same as in cells 2 and 3 (Table 2).

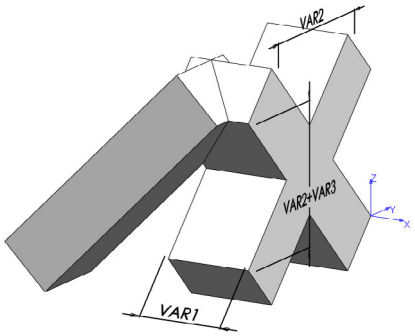

Fig. 12 Cell 4 (two cross bars in the transversal direction and one cross bar in the longitudinal direction)

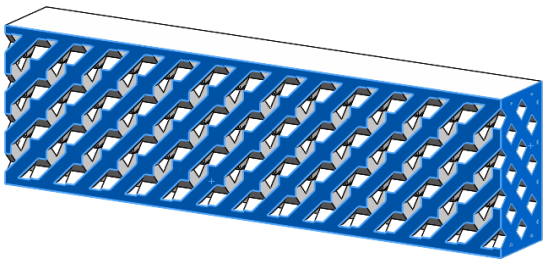

Fig. 13 Sample model with internal structure according to cell 4

2.3.5 Cell 5 (one cross bar in each transversal and longitudinal direction and horizontal bars)

The fifth type of cellular structure was defined keeping only two cross bars from the proposal of cell 2, one in each longitudinal and transverse plane. The bars kept were the ones with direction from the zone of load application to the external faces of the part. Moreover, one horizontal bar was added in the joint between the two cross bars (Fig. 14). The parameterisation and design variables were the same as in the previous case (cell 4). The side of the horizontal bars in the *Z* direction was always 0.5 mm, while the side in the *Y* direction was the same as for the inclined bars (VAR1). The limits of the design variables were the same as in cells 2–4 (Table 2). Fig. 15 shows the geometry obtained with this cell.

2.3.6 Cell 6 (one cross bar in each transversal and longitudinal direction and vertical bars)

The last type of cellular structure was the same as in the previous case, but replacing the horizontal

bar by a vertical one (Fig. 16). Fig. 17 shows the final geometry.

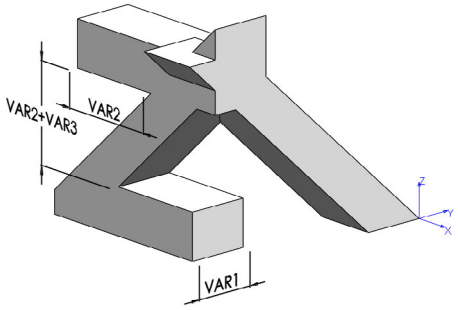

Fig. 14 Cell 5 (one cross bar in each transversal and longitudinal direction and horizontal bars)

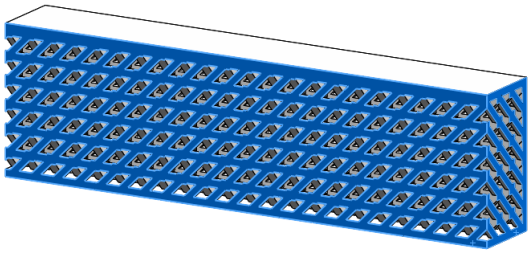

Fig. 15 Sample model with internal structure according to cell 5

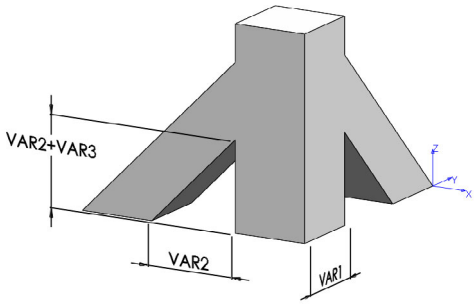

Fig. 16 Cell 6 (one cross bar in each transversal and longitudinal direction and vertical bars)

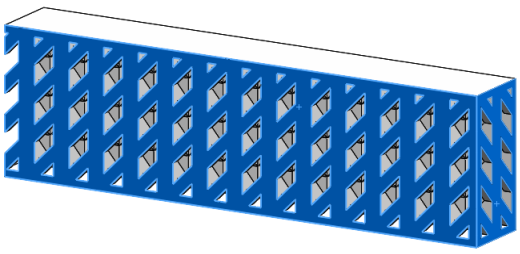

Fig. 17 Sample model with internal structure according to cell 6

The design variables and parameterisation (Fig. 16) were the same as in the previous case (cell 5). The side of the vertical bars was also defined by 'VAR1'. The limits of the design variables were the same as those used in cells 2–5 (Table 2).

2.4 Optimisation

2.4.1 Optimisation method

The new optimisation method consists of three main stages. First of all, a design of experiments (DOE) is applied. This stage consists of selecting a set of sampling points of the domain to be evaluated by FE simulations in order to gather information about the behaviour of the part (vertical displacement of the punch and mass) according to the changes of the design variables. This stage first evaluates three points (design with the minimum, average, and maximum values of the variables, respectively) and afterwards uses two different genetic algorithms (GAs): a GA with binary coding to select n corners (n is the number of design variables), and subsequently another GA with ternary coding to add n more points in the middle of the edges. The binary and ternary codes allow using two and three levels for each design variable, respectively. GAs were used to maximize the distance between the selected sampling point and the previous points already added (to distribute the points all over the search domain). Hermite interpolation was also used to add new sampling points trying to approach the feasible/unfeasible border along one edge of the search domain.

After the initial DOE, the second stage is carried out. This consists of creating a surrogate model based on Kriging with linear and exponential regression and correlation models, respectively. All the sampling points from the previous stage (DOE) are used to create the Kriging metamodel. The aim of this metamodel is to evaluate the fitness function during the evolution of the GAs employed so as to search the optimal design without carrying out FE simulations thus reducing the computational time. The GA is repeated several times. For each run, the best design achieved is simulated by FEM and the results are added in the database to update the metamodel. Some penalization strategies are applied in the first n iterations to lead to new sampling points spread along the feasible/unfeasible border (location of the optimum), thus improving the metamodel accuracy in the relevant areas of the search domain. This stage also includes a final refinement loop so that more sampling

points are added until the metamodel achieves a certain level of accuracy against the predictions (5% error is allowed between the metamodel estimations and the simulation results).

Once the metamodel reaches the required accuracy, a final optimisation is carried out. This last stage uses a standard GA to find the optimal design, supported again by the predictions of the Kriging metamodel created with all the available data gathered in the previous stages. The optimal design obtained by the GA is simulated. If the results show that this design is better than the best design obtained in the previous stages, it will be the final optimum design. Otherwise, the Kriging is updated with the last point simulated and the GA is run again. This is repeated in a loop until the best design from previous stages is improved.

This methodology was implemented and applied, but some limitations were found. As mentioned in Section 2.3, the maximum distance of the horizontal hanging structures was established at 2 mm to guarantee manufacturability. This leads to the definition of small internal structures that increase the CPU time of the geometry updating, increase the probability of geometry errors (zero thickness walls), and also cause more mesh problems. Therefore, the initial optimisation strategy was modified to resolve those problems.

1. The first three points evaluated during the DOE were suppressed to avoid singular geometries that could cause zero thickness error during the optimisation process.

2. The Latin Hypercube DOE was applied instead of using a two-phase GA to determine the location of the sampling points. Latin Hypercube proposes random designs but by exploring all the areas of the domain and adding only one sample in each row and each column of the domain. The main difference is that the previous DOE added sampling points in the corners or middle points of the search domain (three levels for each variable: minimum, medium, and maximum values), leading to singular geometries with a higher probability of causing zero thickness errors. Latin Hypercube DOE works with random values that will not produce these singular geometries. This new DOE was implemented using a Matlab function (MathWorks, 2015) and maximising the minimum distance between points to explore all the zones of the search domain.

3. The Kriging metamodel was modified to use different regression models (Lophaven et al., 2002a, 2002b) depending on the amount of data available. In the previous version, the regression model was always a one-order polynomial, while in this case, the program tries first to generate the metamodel using a two-order regression model. If the number of sampling points or distribution is poor, the algorithm automatically reduces the order of the polynomial until the metamodel is generated. This allows use of the best regression model according to the data available.

4. Since SLM requires small structures to avoid hanging geometries, very small details such as hollows can appear during the optimisation process (Fig. 18), and lead to mesh problems. To solve this limitation, a mesh refinement loop was implemented using two different types of mesher tools available in the CAD/FEM software. Initially, only the curvature-based mesher was used. This mesher automatically refines the mesh elements depending on the geometry. For this reason, it is the most robust mesher as it can successfully discretise many different designs with the same mesh parameters. However, the standard mesher includes a tolerance parameter that simplifies the mesh when there are geometric details smaller than the tolerance value. Therefore, when singular geometries are generated during the optimisation process, the curvature-based mesher may fail, while the standard mesher merges the nodes of the detail and successfully meshes the part. For this reason, the refinement of the mesh was modified. If the curvature-based mesher fails, the program tries it with the standard mesher and, if that also fails, the element size is reduced 10% and the cycle starts again. If the error continues, this refinement is repeated three times in a loop. If the geometry is not meshed after these three iterations, the optimisation program stops (Fig. 19). This strategy allows a more robust optimisation as it can resolve mesh problems generated during the optimisation.

Fig. 20 summarises the general strategy of the optimisation program.

2.4.2 Results of the parametric optimisation

The six cell type geometries were optimized using the new parametric optimisation method described in the previous section. In order to take into account the stochastic characteristics of the

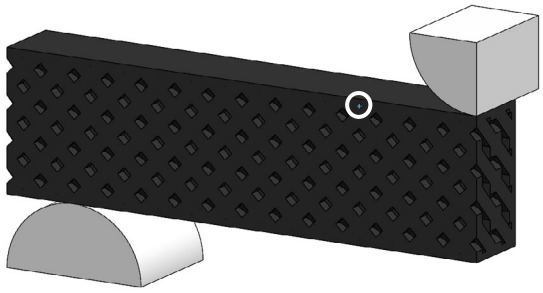

Fig. 18 Small geometry detail of a part (inside the white circle)

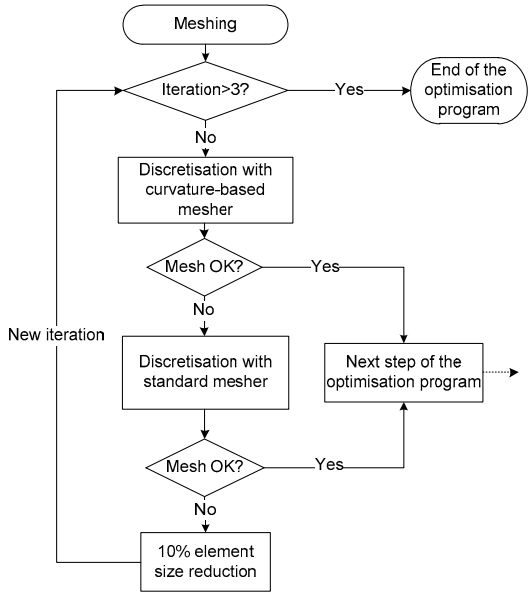

Fig. 19 Flow chart of the mesh refinement implemented in the optimisation program

optimisation method, each case was optimised five times to obtain a mean value of the different results (30 optimisation runs). The mean value of the mass and optimisation time were calculated from the 30 optimums obtained. These average values were used as reference values. Subsequently, the average values of mass and optimisation time for each cell type were evaluated and represented in terms of variation compared with these reference values (Fig. 21).

According to the results observed in Fig. 21, cells 1–3 achieve the best results in terms of weight reduction. Cell 3 obtains the best result, reducing the mass 8% compared with the reference value. However, cells 1 and 2 achieve similar results in mass (5% and 6% of weight reduction, respectively) but with a much lower optimisation time (51% and 30% of time reduction, respectively, against 37% of increasing time for cell 3).

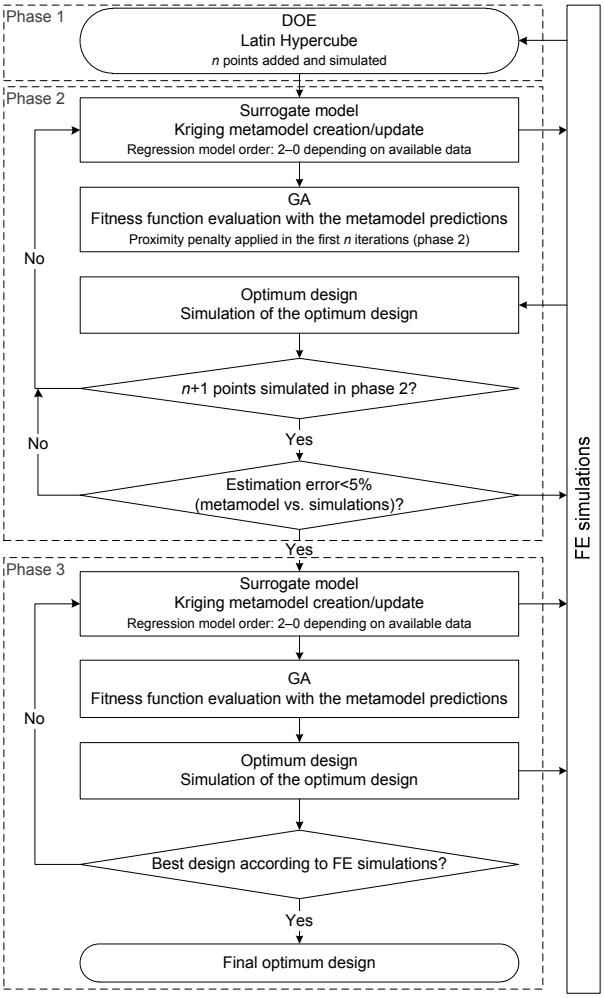

Fig. 20 Flow chart overview of the optimisation strategy

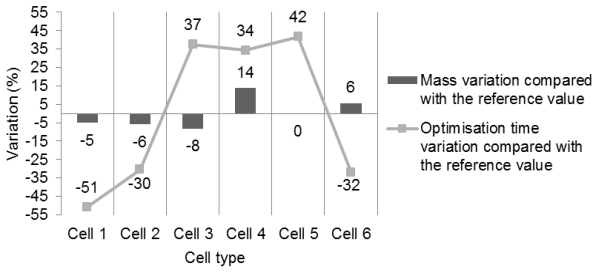

Fig. 21 Variations of mean values of the mass of the optimums and the optimisation time for each cellular geometry compared with the reference values

Among the five different optimums obtained for each one of the cellular geometries, the best one in

terms of weight was selected. Table 3 shows the design variables and relative mass (variation of the mass compared with the reference value) of the optimum selected for each cell typology.

Table 3 Design variables and relative mass of the optimum design selected for each cell type

Cell type	VAR1 (mm)	VAR2 (mm)	VAR3 (mm)	Relative mass (%)
Cell 1	1.24	2.00	1.85	−5.16
Cell 2	1.50	1.49	0.46	−5.46
Cell 3	0.92	1.48	0.00	−8.06
Cell 4	1.17	1.34	0.00	14.49
Cell 5	0.66	1.00	0.00	−2.52
Cell 6	1.16	1.39	0.00	6.70

As the FEM analyses were carried out using double symmetry, the selected geometries were adapted again to the initial dimensions by applying mirror features. Additionally, 2 mm of support structure was applied in the base of the selected geometries to have enough space to cut and separate the parts from the manufacturing platform. Fig. 22 shows the six final geometries and Fig. 23 the sectional views.

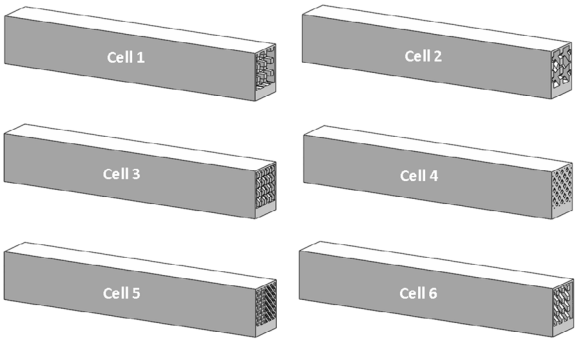

Fig. 22 Final geometries to be manufactured (best optimum of each cell type)

2.5 Reinforced cellular structure and optimisation

Apart from the six geometries shown in Fig. 22, another geometry was proposed to apply the concept of cellular structure and reinforcement. As cell 1 achieved the best combination of weight reduction and optimisation time, this cellular structure was selected and three reinforcement zones were added in the most stressed areas, which are the contact zones of the support and punch tool, including also the lower zone under load. Nine design variables were defined in the reinforced geometry (Fig. 24), the same three as in cell 1 and six more described as follows:

VAR1: side of the square bars (0.5–1.5 mm).

VAR2: distance between bars in the X and Y directions (1–2 mm).

VAR3: distance between bars in the Z direction (1–3 mm).

VAR4: height of the upper reinforcement (0.5–4 mm).

VAR5: angle of the upper reinforcement from the horizontal (45°–80°).

VAR6: height of the lower reinforcement (0.5–4 mm).

VAR7: length of the lower reinforcement (0.5–8 mm).

VAR8: length of the reinforcement in the support zone (1–8 mm).

VAR9: height of the reinforcement in the support zone (0.5–4 mm).

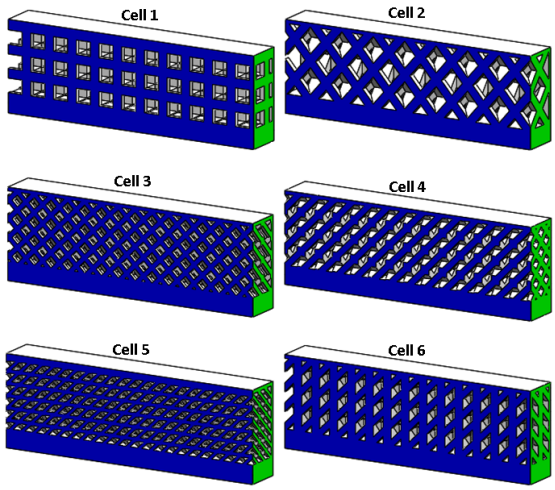

Fig. 23 Sectional views of the geometries selected

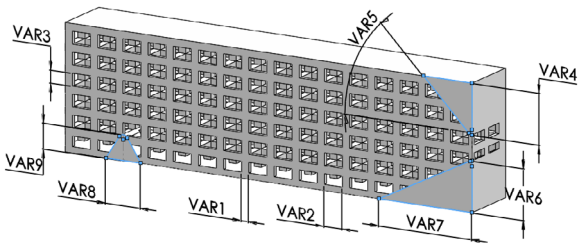

Fig. 24 Design variables of the reinforced cellular geometry (cell 1 reinforced)

This reinforced geometry was optimised five times and the average variations of mass and optimisation time (compared with the reference values) are represented in Fig. 25.

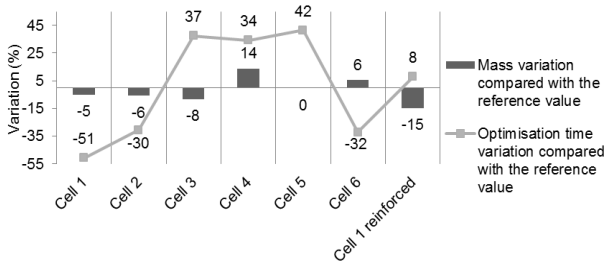

Fig. 25 Variations of the mass and optimisation time averages of each cellular geometry compared with the reference values

The reinforced geometry achieves the highest reduction of weight (15%). Regarding the optimisation time, it was much higher than for cell 1 because of the greater number of design variables. However, it is even lower than the optimisation times of cell 3 (37%), cell 4 (34%), and cell 5 (42%).

Among the five optimums achieved, the best one in terms of mass was selected for manufacture. Table 4 shows the dimensions of the design variables and Fig. 26 the longitudinal section of the final geometry with 2 mm of support in the base.

Table 4 Design variables and relative mass of the optimum design selected of the cell 1 reinforced geometry

Parameter	Value	Parameter	Value
VAR1 (mm)	0.5	VAR6 (mm)	4
VAR2 (mm)	1	VAR7 (mm)	8
VAR3 (mm)	1.3	VAR8 (mm)	8
VAR4 (mm)	4	VAR9 (mm)	0.5
VAR5 (°)	45	Relative mass (%)	−14.26

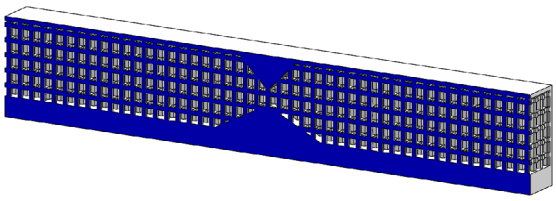

Fig. 26 Section view of the final reinforced geometry (cell 1 reinforced)

2.6 Manufacturing of the parts and mechanical tests

The geometries selected in the previous section (cells 1–6 and the reinforced geometry) were saved as STL and located-oriented in the manufacturing platform using the Phenix Processing 3.3.6 software (Fig. 27).

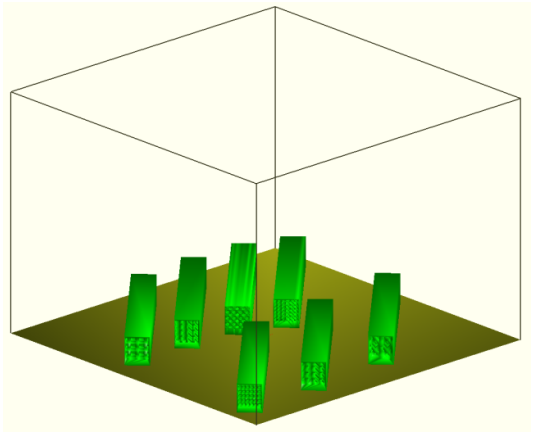

Fig. 27 Location of the seven parts in the manufacturing platform (Phenix Processing 3.3.6 software)

The layer thickness was 30 μm, the total number of layers was 400 and the power of the laser was 300 W. The material used was Ti6Al4V and the SLM machine was a Phenix ProX200. The manufacturing process lasted 375.3 min. Once the build platform was cleaned and removed from the machine, the parts were cleaned in an ultrasonic bath to remove internal powder. The parts were then separated from the build platform using wire-cut electrical discharge machining. Fig. 28 shows the parts obtained. The finishing of the ends of the cell 6 part was not good because the first layer of these bars had no solid support or connection with the rest of the part. Therefore, it is deduced that the roller may have displaced the first layer of the bar during the powder loading.

The samples were ground to remove the support material placed under the base of the samples. Subsequently, the samples were measured at three different points (the ends and the middle point) to determine the real height and width. Three measurements were taken from each sample and dimension to obtain the average values. The parts were also weighed (Table 5).

Subsequently, the samples were tested under flexural load in a PB2 MicroTest machine (three-point bending flexural test). The speed of the load application was 5 mm/min and the separation between supports 60 mm (the same distance as used in the simulations) (Fig. 29). The frequency of data registration was 50 Hz.

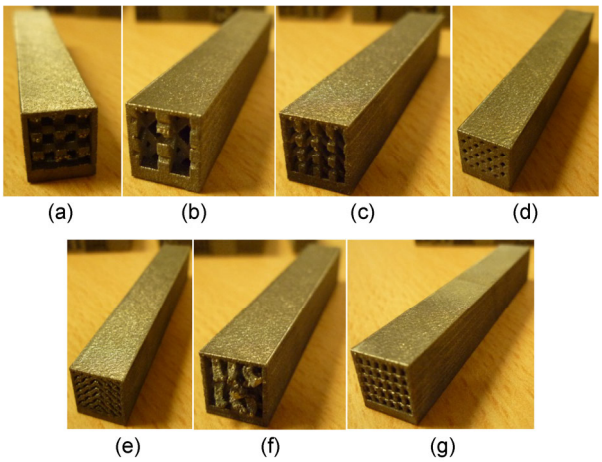

Fig. 28 Cell 1 (a), cell 2 (b), cell 3 (c), cell 4 (d), cell 5 (e), cell 6 (f), and cell 1 reinforced (g) parts

Table 5 Dimensions and mass of the parts (theoretical dimensions are 10 mm×10 mm in height and width)

Sample	Average height (mm)	Average width (mm)	Mass (g)
Cell 1	10.264	10.323	18.492
Cell 2	10.241	10.302	17.853
Cell 3	10.353	10.289	19.698
Cell 4	10.304	10.289	22.460
Cell 5	10.292	10.287	21.345
Cell 6	10.345	10.323	21.241
Cell 1 reinforced	10.305	10.326	19.155

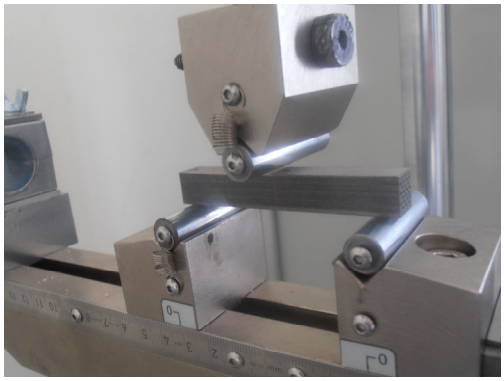

Fig. 29 Flexural test

3 Results

A linear regression of the force-displacement curve was carried out to obtain the stiffness of each sample (slope of the linear equation). The results obtained are summarised in Table 6.

Fig. 30 shows the deviation of specific stiffness of each design compared with the reference value. The reference value is the mean value of all the samples except cell 1 reinforced. Both the real and simulated results are depicted.

The differences between the real and simulated specific stiffnesses in Fig. 30 were calculated, as shown in Fig. 31. The positive values represent the

Table 6 Stiffnesses of the samples

Sample	Stiffness (N/mm)
Cell 1	5261.5
Cell 2	5560.3
Cell 3	5937.8
Cell 4	5599.7
Cell 5	5934.7
Cell 6	5949.2
Cell 1 reinforced	5685.4

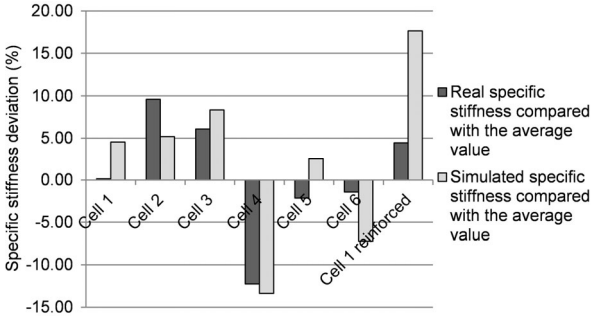

Fig. 30 Specific stiffness deviation compared with the average value (real and simulated values)

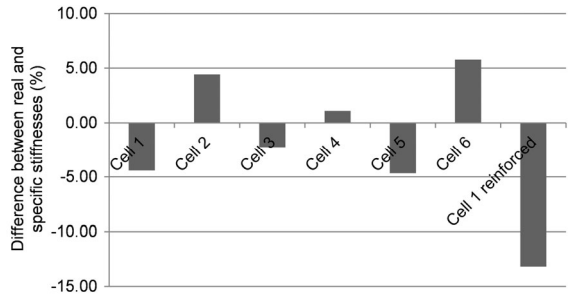

Fig. 31 Differences between the real and simulated specific stiffnesses compared with the average value

cases in which the experimental specific stiffness exceeds the simulated estimation. The negative values appear when the real specific stiffness is lower than the simulated one.

4 Discussion

According to the results, the best in terms of specific stiffness was obtained for "cell 1 reinforced", as was expected from the simulations. However, some variance was found between the expected results obtained through FE simulations and the real results (Fig. 31). These differences may be caused by manufacturing imperfections related to the SLM process and to the wire-cut electrical discharge machining (samples with different heights despite the subsequent grinding). According to Labeas and Sunaric (2010), the accuracy of the FE model is highly dependent on the strut geometrical characteristics and especially the cross-sectional radius of the final part. Therefore, the exact correlation between simulated and real results in 3D printed parts is difficult to achieve.

Through a deeper analysis of Fig. 31, it can be observed that the simulations overestimated the results mainly for cell 1, cell 5, and cell 1 reinforced. These samples were precisely the ones with horizontal bars in the cell pattern (horizontal hanging structures), which means that the loss of mechanical properties compared with the simulations may be caused by the more difficult manufacturing conditions associated with horizontal hanging structures. The first layer of each horizontal bar is sintered without a complete solid base in the hanging areas. Therefore, the laser may displace the powder in the hanging areas of this layer (Fig. 32) during the sintering, leading to reduced mechanical properties. As depicted in Fig. 31, "cell 1 reinforced" is the part with the highest loss of stiffness compared with the simulation results. This part is also the one with the highest number of areas without solid support beneath. On the other hand, "cell 5" and "cell 1" have a similar area of horizontal bars without solid support beneath, and that is the reason why the loss of stiffness compared with the FEM results is similar between them.

To evaluate whether there is a correlation between the area of horizontal bars without solid support beneath and the loss of specific stiffness compared with the simulation results, this area was calculated for the parts of cell 1, cell 5, and cell 1 reinforced. In order to compare these values with Fig. 31, a reference area was calculated to evaluate the percentage of hanging areas compared to it. Therefore, this reference value was adjusted to obtain 13.2% in the case of cell 1 reinforced. By using this reference, the percentages of cell 1 and cell 5 were also assessed and depicted in Fig. 33. It can be noted that there is correlation between the loss of specific stiffness (difference between simulations and experimental results) and the number of horizontal hanging areas.

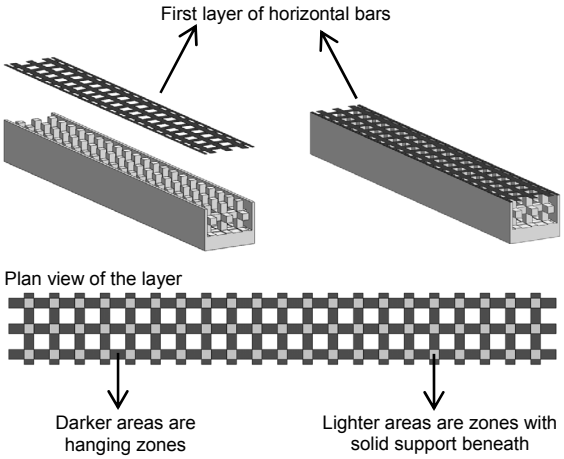

Fig. 32 Layer without solid support beneath

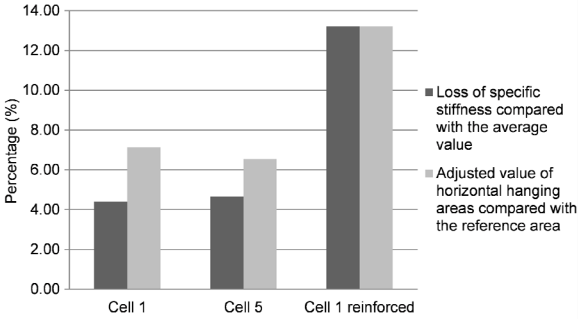

Fig. 33 Correlation of the loss of specific stiffness with the horizontal hanging areas

The accuracy of the actual fabricated work with respect to the original CAD design parts was not considered in this study. This difference is difficult to

control as it depends on many factors such as the geometry itself, the accuracy of the STL file (Calignano, 2018), the laser power, the powder quality, and the machine accuracy. The difference between the initial CAD model and the STL file can be easily reduced by replacing the STL file by the additive manufacturing file (AMF, more accurate definition). Regarding the process parameters, Sing et al. (2018) proposed some polynomial equations for estimating the actual fabricated strut dimensions depending on the laser power, scanning speed, and layer thickness. Although the mathematical models were calculated for a unique strut geometry and material, the same procedure could be applied to extend the study and obtain some global mathematical expressions that could be implemented by this methodology. These equations could be introduced in the equation manager and be applied to calculate the actual dimensions of the strut depending on the selected manufacturing parameters and the theoretical design value. In future work, compensation strategies (Bagheri et al., 2017) could be also implemented to reduce the mismatch between the initial CAD model and the final manufactured part, and thus reduce the difference between the simulated and experimental results.

5 Conclusions

This study presents a new optimisation algorithm that has been developed for the lightweight parametric optimisation of SLM parts. The methodology has been tested to optimise six different types of cell structures and it overcomes the limitations described in Section 2.4.1.

From the study of the different cell typologies it can be concluded that the cubic cell pattern has some advantages in terms of CAD definition, parameterisation, and optimisation time. The simplicity of the geometry reduces the design and preconditioning time. Moreover, the updating of the geometry during the optimisation is also much faster compared with other cell structures. On the other hand, the quality of the optimums reached with cubic cells is close to the best designs achieved with other more complex cells. However, cubic cell structures have horizontal bars without solid support material beneath (hanging structures). This causes a loss of mechanical properties compared with the estimates of the finite element analysis.

The combination of cubic cellular structures with user-defined and parameterised reinforcements allows the achievement of more efficient designs (higher specific stiffness) but it also involves longer optimisation time derived from the use of more design variables.

This methodology can be applied in several sectors, especially in those where the SLM technology has a high potential. Among them, tissue engineering is considered a promising field because cellular structures are needed to promote the cell proliferation and tissue regeneration. In that sense, this approach could be also adapted and extended to other AM technologies (or even combined with innovative materials) to find new solutions for the medical sector, such as improved scaffolds for osteoarthritis (Monzón, 2018).

References

Akin JE, Arjona-Baez J, 2001. Enhancing structural topology optimization. *Engineering Computations*, 18(3-4):663-675. https://doi.org/10.1108/02644400110387640

Aremu A, Ashcroft I, Wildman R, et al., 2013. The effects of bidirectional evolutionary structural optimization parameters on an industrial designed component for additive manufacture. *Proceedings of the Institution of Mechanical Engineers, Part B: Journal of Engineering Manufacture*, 227(6):794-807. https://doi.org/10.1177/0954405412463857

Autodesk, 2015. Netfabb Software: Additive Manufacturing and Design Software. Autodesk. http://www.netfabb.com/

Autodesk Within, 2015. Within–Software–General Overview. Autodesk. http://withinlab.com/software/

Bagheri ZS, Melancon D, Liu L, et al., 2017. Compensation strategy to reduce geometry and mechanics mismatches in porous biomaterials built with selective laser melting. *Journal of the Mechanical Behavior of Biomedical Materials*, 70:17-27. https://doi.org/10.1016/j.jmbbm.2016.04.041

Calignano F, 2018. Investigation of the accuracy and roughness in the laser powder bed fusion process. *Virtual and Physical Prototyping*, 13(2):97-104. https://doi.org/10.1080/17452759.2018.1426368

Campanelli SL, Contuzzi N, Angelastro A, et al., 2010. Capabilities and performances of the selective laser melting

process. *In*: Er MJ (Ed.), New Trends in Technologies: Devices, Computer, Communication and Industrial Systems. InTech, p.233-252.

Dassault Systèmes, 2013. SOLIDWORKS Help: Node to Surface Contact. Dassault Systèmes. http://help.solidworks.com/2013/English/SolidWorks/cworks/c_Node_to_Surface_Contact.htm

Dotcheva M, Thomas D, Millward H, 2009. An evaluation of rapid manufactured cellular structures to enhance injection moulding tool performance. *International Journal of Materials Engineering and Technology*, 1(2):105-127.

Gibson I, Rosen DW, Stucker B, 2009. Additive Manufacturing Technologies: Rapid Prototyping to Direct Digital Manufacturing. Springer, New York, USA.

González SG, 2010. SolidWorks Simulation. RA-MA S.A., Madrid, Spain (in Spanish).

Hutmacher DW, Sittinger M, Risbud MV, 2004. Scaffold-based tissue engineering: rationale for computer-aided design and solid free-form fabrication systems. *Trends in Biotechnology*, 22(7):354-362. https://doi.org/10.1016/j.tibtech.2004.05.005

ISO/ASTM International, 2015. Additive Manufacturing—General Principles—Terminology, ISO/ASTM 52900: 2015. ISO/ASTM International, Switzerland.

Jorge MA, da Conceicao Batista F, Almeida HA, et al., 2007. Virtual and Rapid Manufacturing: Advanced Research in Virtual and Rapid Prototyping. CRC Press, Boca Raton, USA.

Kranz J, Herzog D, Emmelmann C, 2015. Design guidelines for laser additive manufacturing of lightweight structures in TiAl6V4. *Journal of Laser Applications*, 27(S1): S14001. https://doi.org/10.2351/1.4885235

Kulkarni VR, Tambe AG, 2013. Optimization and finite element analysis of steering knuckle. Proceedings of Altair Technology Conference.

Labeas GN, Sunaric MM, 2010. Investigation on the static response and failure process of metallic open lattice cellular structures. *Strain*, 46(2):195-204. https://doi.org/10.1111/j.1475-1305.2008.00498.x

Lophaven SN, Nielsen HB, Søndergaard J, 2002a. DACE–a Matlab Kriging Toolbox, Version 2.0. IMM-TR-2002-12, Technical University of Denmark, Kongens Lyngby, Denmark.

Lophaven SN, Nielsen HB, Søndergaard J, 2002b. Aspects of the Matlab Toolbox Dace. IMMREP-2002-13, Technical University of Denmark, Kongens Lyngby, Denmark.

Lynch ME, Gu WJ, El-Wardany T, et al., 2013. Design and topology/shape structural optimisation for additively manufactured cold sprayed components. *Virtual and Physical Prototyping*, 8(3):213-231. https://doi.org/10.1080/17452759.2013.837629

Materialise 3-matic, 2015. Materialise 3-matic Lightweight Structures Module. Materialise 3-matic. http://software.materialise.com/3-matic-lightweight-structures-module

MathWorks, 2015. Lhsdesign: Latin Hypercube Sample. MathWorks, Spain. http://es.mathworks.com/help/stats/lhsdesign.html

Monzón M, 2018. Biomaterials and additive manufacturing: osteochondral scaffold innovation applied to osteoarthritis (BAMOS project). *Journal of Zhejiang University-SCIENCE A (Applied Physics & Engineering)*, 19(4): 329-330. https://doi.org/10.1631/jzus.A18NW001

Mullen L, Stamp RC, Brooks WK, et al., 2009. Selective laser melting: a regular unit cell approach for the manufacture of porous, titanium, bone in-growth constructs, suitable for orthopedic applications. *Journal of Biomedical Materials Research Part B: Applied Biomaterials*, 89B(2): 325-334. https://doi.org/10.1002/jbm.b.31219

Murr LE, Gaytan SM, Medina F, et al., 2010. Next-generation biomedical implants using additive manufacturing of complex, cellular and functional mesh arrays. *Philosophical Transactions of the Royal Society A: Mathematical, Physical and Engineering Sciences*, 368(1917): 1999-2032. https://doi.org/10.1098/rsta.2010.0010

Peltola SM, Melchels FP, Grijpma DW, et al., 2008. A review of rapid prototyping techniques for tissue engineering purposes. *Annals of Medicine*, 40(4):268-280. https://doi.org/10.1080/07853890701881788

Pepelnjak T, Gantar G, Kuzman K, 2001. Numerical simulations in optimisation of product and forming process. *Journal of Materials Processing Technology*, 115(1):122-126. https://doi.org/10.1016/S0924-0136(01)00744-0

Protasov CE, Khmyrov RS, Grigoriev SN, et al., 2017. Selective laser melting of fused silica: interdependent heat transfer and powder consolidation. *International Journal of Heat and Mass Transfer*, 104:665-674. https://doi.org/10.1016/j.ijheatmasstransfer.2016.08.107

Sachlos E, Czernuszka JT, 2003. Making tissue engineering scaffolds work. Review: the application of solid freeform fabrication technology to the production of tissue engineering scaffolds. *European Cells and Materials*, 5:29-40.

Salmi A, Calignano F, Galati M, et al., 2018. An integrated design methodology for components produced by laser powder bed fusion (L-PBF) process. *Virtual and Physical Prototyping*, 13(3):191-202. https://doi.org/10.1080/17452759.2018.1442229

Siemens PLM Software, 2010. Femap Version 10.2: What's New. Siemens PLM Software. https://appliedcax.com/support-and-training/technical-online-seminars/seminars/2010-12-02_seminar.pdf

Sing SL, Yeong WY, Wiria FE, et al., 2017. Direct selective laser sintering and melting of ceramics: a review. *Rapid Prototyping Journal*, 23(3):611-623. https://doi.org/10.1108/RPJ-11-2015-0178

Sing SL, Wiria FE, Yeong WY, 2018. Selective laser melting

of lattice structures: a statistical approach to manufacturability and mechanical behavior. *Robotics and Computer-Integrated Manufacturing*, 49:170-180. https://doi.org/10.1016/j.rcim.2017.06.006

Synopsys, 2015. Simpleware Software Solutions: 3D Image Data Visualization, Analysis and Model Generation with Simpleware. Synopsys. http://www.simpleware.com

Thomas D, 2009. The Development of Design Rules for Selective Laser Melting. PhD Thesis, University of Wales, Cardiff, UK.

Wohlers T, Caffrey T, 2014. Wohlers Report 2014: 3D Printing and Additive Manufacturing State of the Industry Annual Worldwide Progress Report. Wohlers Associates, Fort Collins, USA.

Wong KV, Hernandez A, 2012. A review of additive manufacturing. *ISRN Mechanical Engineering*, 2012:208760. https://doi.org/10.5402/2012/208760

Yang SF, Leong KF, Du ZH, et al., 2001. The design of scaffolds for use in tissue engineering. Part I. Traditional factors. *Tissue Engineering*, 7(6):679-689. https://doi.org/10.1089/107632701753337645

Yap CY, Chua CK, Dong ZL, et al., 2015. Review of selective laser melting: materials and applications. *Applied Physics Reviews*, 2(4):041101. https://doi.org/10.1063/1.4935926

Yeong WY, Chua CK, Leong KF, et al., 2004. Rapid prototyping in tissue engineering: challenges and potential. *Trends in Biotechnology*, 22(12):643-652. https://doi.org/10.1016/j.tibtech.2004.10.004

Yoo DJ, 2011. Computer-aided porous scaffold design for tissue engineering using triply periodic minimal surfaces. *International Journal of Precision Engineering and Manufacturing*, 12(1):61-71. https://doi.org/10.1007/s12541-011-0008-9

Zhang K, Liu TT, Liao WH, et al., 2018. Influence of laser parameters on the surface morphology of slurry-based Al_2O_3 parts produced through selective laser melting. *Rapid Prototyping Journal*, 24(2):333-341. https://doi.org/10.1108/RPJ-12-2016-0201

中文概要

题　目：通过新型轻量化参数优化方法比较激光选区熔化部件设计的不同细胞结构

目　的：1. 提出一种在外型不变的部件内模拟不同细胞结构的方法；2. 发展激光选区熔化（SLM）部件轻量化参数设计的新方法；3. 利用这一方案实现优化设计并比较不同细胞结构的质量。

创新点：1. 提出基于拉丁超立方实验设计、遗传算法、克里金元模型和有限元方法的轻量化优化方案；2. 该方法可通过较少的采样获得良好的结果并能克服几何奇点（内部网格细化算法）的问题。

方　法：1. 进行内部细胞结构的生成和参数化；2. 根据输入数据（设计变量和约束条件等）采用拉丁超立方实验设计模拟所选样本；3. 利用先前的数据创建克里金元模型并利用预测的元模型来计算遗传算法演化过程中的适应函数；4. 将模拟实现的优化结果添加到数据中更新元模型，并通过数次重复迭代提高元模型的准确度直至误差小于5%；5. 将这一概念应用于不同的几何结构，然后通过 SLM 加工制造优化后的几何结构，并在弯曲载荷下进行测试。

结　论：1. 该优化算法通过适当的参数化克服了 SLM 技术的相关限制，可适用于 SLM 部件的优化；2. 立方单元格在计算机辅助设计定义、参数化和时间优化等方面有一些优势，但和有限元分析的估计结果相比，其存在的缺乏坚实支撑的水平条（悬挂结构）会造成机械性能损失；3. 将立方单元结构与用户自定义的参数化增强相结合可以得到更有效的设计结果（更高的比刚度），但更多的设计变量也延长了所需要的优化时间。

关键词：参数优化；细胞结构；激光选区熔化；有限元分析；实验设计；精细化